A chemotaxis model of feather primordia pattern formation during avian development

Kevin J. Painter[a,b], William Ho[c], Denis J. Headon[c]

[a]*Department of Mathematics & Maxwell Institute for Mathematical Sciences, Heriot-Watt University, Edinburgh, UK, K.Painter@hw.ac.uk*
[b]*Dipartimento di Scienze Matematiche, Politecnico di Torino, Torino, Italy*
[c]*Roslin Institute & Royal (Dick) School of Veterinary Studies, University of Edinburgh, UK*

Abstract

The orderly formation of the avian feather array is a classic example of periodic pattern formation during embryonic development. Various mathematical models have been developed to describe this process, including Turing/activator-inhibitor type reaction-diffusion systems and chemotaxis/mechanical-based models based on cell movement and tissue interactions. In this paper we formulate a mathematical model founded on experimental findings, a set of interactions between the key cellular (dermal and epidermal cell populations) and molecular (fibroblast growth factor, FGF, and bone morphogenetic protein, BMP) players and a medially progressing priming wave that acts as the trigger to initiate patterning. Linear stability analysis is used to show that FGF-mediated chemotaxis of dermal cells is the crucial driver of pattern formation, while perturbations in the form of ubiquitous high BMP expression suppress patterning, consistent with experiments. Numerical simulations demonstrate the capacity of the model to pattern the skin in a spatial-temporal manner analogous to avian feather development. Further, experimental perturbations in the form of bead-displacement experiments are recapitulated and predictions are proposed in the form of blocking mesenchymal cell proliferation.

Keywords: Pattern formation; Morphogenesis; Feather placodes; Chemotaxis and Turing models

1. Introduction

1.1. Theoretical background

The mechanisms that allow an embryo to self-pattern into a fully formed and functioning organism remain the subject of considerable speculation. Theoretical models for pattern formation have been developed from several viewpoints (for recent reviews, e.g. [1, 2, 3, 4]). Pre-pattern models, such as the "French-flag" model of positional information [5], suppose that structure arises iteratively through pattern building on pattern. On the other hand, self-organising models make no *a priori* assumption of previous pattern: structures can emerge from the inherent noise in an essentially homogeneous (uniform) tissue.

These self-organising or "symmetry-breaking" models can be further subdivided, for example into chemical- or cell-based. The well known Turing mechanism [6, 7] is an example of the former, with its principal assumption being the existence of a network of reacting and diffusing chemical morphogens. In its simplest form it can be understood through the concept of short-range activation and long-range inhibition [7, 8], where one component plays the role of an "activator" that directly (or indirectly) upregulates its own activity (i.e. autocatalysis) while also promoting an "inhibitor" that acts to limit the activator's activity. If activation operates on a shorter spatial range, for example via lower molecular diffusion, these

processes combine to generate a spatially periodic morphogen distribution that can provide a template for tissue patterning. Recent years have witnessed a growing number of systems where reaction-diffusion type principles are proposed to operate, including skin morphogenesis [9, 10, 11, 12], tooth morphogenesis [13], tracheal patterning [14], generation of left-right asymmetry [15] and limb patterning [16].

In cell movement and mechanical models it is the properties of cells and their mechanical interactions with the surrounding tissue that generate patterning. Classical chemotaxis models [17] describe the directed movement of cells in response to chemical attractants (or repellents) and predict the organisation of a population into clustered structures: self-organisation of dispersed *Dictyostelium discoideum* cells into aggregation mounds is founded on a chemotactic response to self-secreted cAMP [18]. Chemotaxis has been implicated in various developmental process, including chick gastrulation [19], neural crest migration [20] and, of particular relevance here, feather development [21].

Avian feather formation offers a classic example of embryonic patterning. During skin development these structures emerge via molecular signalling and tissue crosstalk leading to localised cell condensates that subsequently bud into feathers. Pattern formation occurs at numerous levels and stages, from the spatiotemporal process that lays out a pattern of "primordia" across the skin's surface (Figure 1A) to the within-bud patterning that leads to an intricate and pigmented feather. The skin's accessibility coupled to the diversity of feather patterns across the natural world offers an elegant model system for understanding how pattern can arise and evolve [3].

Earlier theoretical works pre-dated molecular-level understanding: models typically relied on a central self-organising mechanism, such as mechano-chemical interactions (e.g. [22]), reaction-diffusion (e.g. [23]) or a combination of the two (e.g. [24, 25, 26]). Activator-inhibitor (AI) principles proved particularly influential when it came to resolving the core molecular components controlling patterning [9, 27, 28], and recent studies have formally linked experiment and theory such that model variables describe specific molecular components/cell populations and simulations can be tested against experimental observations [29, 10, 30, 21, 31].

1.2. Biological background

The skin serves as a barrier and carries various appendages, including feathers, hairs, nails, scales and glands, which begin their development during embryonic growth. The most numerous appendages, such as hairs, feathers and scales, are rapidly laid out in a periodic pattern that, for many organisms, covers the vast majority of the skin surface. The process of defining the locations of these appendages involves communication between the two tissue layers of the skin, see Figure 1B; the ectoderm-derived epidermis is an epithelial sheet laden with cell-cell physical contacts that restrict movement, while the mesoderm or neural crest-derived mesenchyme called dermis features unconnected cells loosely embedded in a matrix of their own production, thus capable of relatively unrestricted movement.

Definition of the feather pattern begins in chicken embryos around embryonic day 7 (E7.0) and, by hatch at 21 days post egg laying, culminates in a downy plumage. Each presumptive feather is first indicated by a tighter packing of ectodermal cells (a placode) underlaid by a prominent aggregation of dermal mesenchymal cells (a condensate), see Figure 1B. These morphological rearrangements are accompanied by altered gene expression (see Figure 1C) such that a number of genes with initially diffuse expression become focalised and intensified in either the feather primordium (epithelial or mesenchymal component) or restricted in expression to the inter-feather zone. The feather primordium begins rapid proliferation to bud outwards and produce a filament, which then branches to generate the mature feather structure [32].

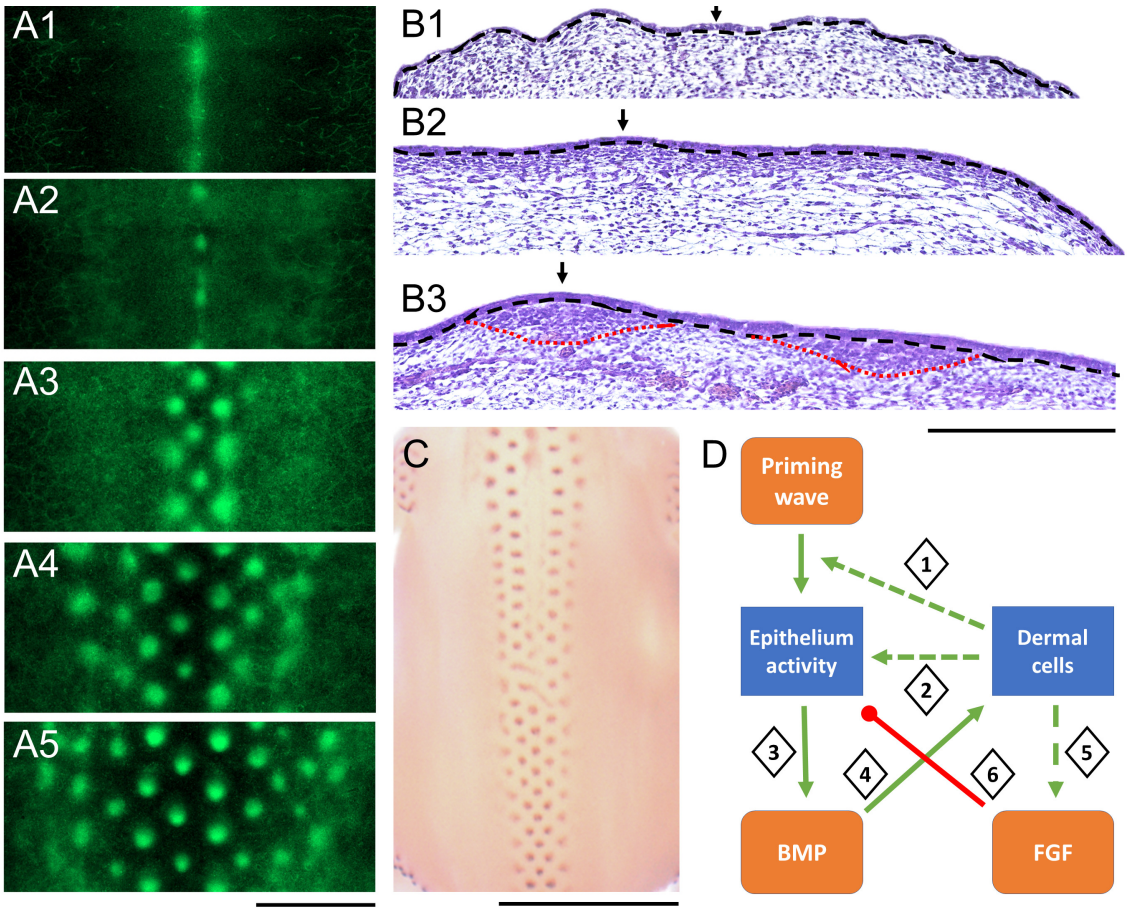

Figure 1: (A) Feather primordia form across the skin in a coordinated spatiotemporal manner, visualised by the sequential formation of discrete dermal cell condensates (localised regions of intense green) in bi-lateral tracts that extend laterally from the dorsal midline. Skin explants prepared from the dorsal tracts of E6.5 GFP chicken embryos, with stills in (A1-A5) taken at 8 hourly intervals from 0 to 32 hours (Scale bar = 1 mm). In each frame, anterior to posterior runs from top to bottom, lateral to medial to lateral from left to right. (B) Histological cross-sections showing skin development at: (B1) E5.5, showing a sparsely populated underlying dermis; (B2) E6.5, displaying a medial to lateral decreasing gradient of dermal cell density; and (B3) E8.5 days, showing individual primordia visualised as discrete dermal cell aggregates (enclosed by red dotted lines). Black dashed lines indicate the epidermal-dermal boundary, black arrows the dorsal midline and scale bar = 200 μm. (C) Expression of *FGF20* along dorsal embryo (scale bar = 2.5 mm). Wholemount in situ detection of *FGF20* RNA transcripts in E7.5 chicken embryos. The darker spots showing gene expression lie within developing feather primordia. Expression of *BMP* shows similar localisation (data not shown). Anterior to posterior runs from top to bottom, lateral to medial to lateral from left to right. (D) A "signalling network" summarising the key interactions incorporated into the mathematical model: (1,2) Dermal cells stimulate epithelium activation, where a priming wave lowers the critical dermal density at which this occurs; (3) Activated epithelium secretes FGF protein; (4) FGF induces positive chemotaxis of dermal cells; (5) Clustered dermal cells secrete BMP protein; (6) BMP inactivates epithelium.

The density of cells in dermal mesenchyme varies in different body locations and at different stages of development. Initially all skin has a low mesenchymal cell density ("loose dermis"), but in regions that will carry feathers this becomes more dense prior to pattern formation. From experimental recombination of mesenchyme and ectoderm from different body sites it has been established that a highly cellular dermis ("dense dermis") is essential to permit pattern formation [33].

The process of primordium patterning begins at stereotypical sites on the embryo, the most well studied being that running along the dorsal midline (spine). Here a stripe of high cell density first forms before breaking into a periodic pattern of aggregates (Figure 1A). Subsequent waves of primordium formation spread bilaterally across the embryo, sequentially generating a pair of newly patterned rows (Figure 1A) at approximately 8 hour intervals and terminating before the entire embryo has become populated with feather primordia. This initial phase of patterning yields an embryo that features feather bearing regions (tracts) and non-feathered regions (apteria) and, throughout this two day patterning process, a periodic spacing between each feather primordium is maintained. Embryonic chicken skin isolated from embryos at E6.5 and cultured (Figure 1A) progresses through the stages of pattern formation at approximately the same rate as in ovo, though the rapid lateral skin expansion that occurs in embryos does not happen in culture [34].

A number of intercellular signalling molecules with an influence on feather patterning have been identified through directed experiments based on selected candidate molecules with widespread developmental roles, and from genetic studies of variation in feather coverage in different chicken lines. Together this work has confirmed a crucial role for fibroblast growth factor (FGF) signalling in promoting cell condensation and consequent feather primordium development, and identified bone morphogenetic (BMP) family members as inhibitors of feather primordium formation [35, 36]. The FGF and BMP families are gene-encoded proteins which are secreted from producing cells into the extracellular space where they can diffuse, interact with extracellular matrix components, and bind to receptors of neighbouring cells to alter the behaviour of receiving cells.

The loss of function of a specific FGF family member, FGF20, underlies the absence of feathers and scales in the 'scaleless' line of mutant chickens [37]. This factor is expressed specifically in the ectoderm but predicted to be capable of diffusing and binding to receptors on adjacent ectodermal and mesenchymal cells. Increased production of a BMP family member underlies the Naked neck trait, which is characterised by absence of neck feathers and reduced tract width on the body [31]. A computational approach to interpret the mechanism underlying selective loss of neck feathering employed a reaction-diffusion network, with FGFs and BMPs respectively fulfilling the generic roles of activator and inhibitor, and the experimental observations regarding the distinction between neck and body, and the role of retinoic acid, could be captured by this approach [31, 3]. In addition, the production of FGF20 [37] and BMP family members [9, 30] in placodes and condensates matches simple reaction-diffusion predictions regarding the site of production of activator and inhibitor. Thus a reaction-diffusion system appeared to capture pattern behaviour and transitions as known at the time.

1.3. Aims of the paper

Despite its predictive success, definitive evidence that an AI type mechanism operates at the base of feather placode formation remains uncertain. For example, simple AI models demand some form of self-enhancement and whether FGF (or any other component) possess the necessary feedbacks remains uncertain. Further, recent experimental data have revealed the importance of mesenchymal compaction during pattern formation, with initial cell rearrangements into nascent clusters triggering gene expression changes

in nearby cells to those of the bud identity [38]. Given these uncertainties, it is necessary to consider other mechanisms that could drive the patterning process.

In the present paper we expand the FGF/BMP based model of [31, 3] through a more detailed representation of cellular and molecular signalling interactions. Specifically, we formulate and analyse a coupled chemotaxis/molecular signalling model for feather development. Section 2 describes the model, which includes variables for the mesenchymal cells in the developing dermis, the activity of the overlying epithelium and the key molecular components FGFs and BMPs. Section 3 summarises the mathematical and numerical analyses used to demonstrate the model's capacity to generate pattern formation consistent with feather organisation, as well as it's ability to recapitulate certain experimental perturbations. We conclude with a discussion, addressing model shortcomings and highlighting areas for future focus.

2. Methods

Our model formalises the biologically-motivated schematic of Figure 1D and consists of a patterning system of partial-differential equations driven by an imposed priming wave. The key assumptions are based on the following set of observations:

1. A mediolaterally-spreading priming wave raises the skin's pattern forming capability [39];
2. Elevated local dermal cell density leads to local epithelium activation [39];
3. Activated epithelium secretes FGF, which diffuses into the mesenchymal layer;
4. FGF induces positive chemotaxis of dermal cells [40, 21];
5. Clustering of dermal cells triggers their secretion of diffusible BMP [38];
6. BMP deactivates epithelium [39].

2.1. Chemotaxis models

Continuous models for chemotaxis are often founded on the well-known Patlak-Keller-Segel (PKS) equations ([41, 17, 42], see also [43]). In a simple model, if $c(\mathbf{x}, t)$ describes the density distribution of a chemotactic cell population at position $\mathbf{x}$ and time t, and $a(\mathbf{x}, t)$ is the concentration of a chemical chemoattractant:

$$\frac{\partial c}{\partial t} = \nabla \cdot (D_c \nabla c - c\chi \nabla a) \; ; \tag{1}$$

$$\frac{\partial a}{\partial t} = D_a \nabla^2 a + \mu c - \delta a \, . \tag{2}$$

Terms on the right hand side of the first equation describe random motility (e.g. imperfect chemotactic steering) with coefficient D_c and chemotactic movement up the gradient of chemoattractant with chemotactic sensitivity coefficient χ. The chemoattractant is assumed to diffuse with diffusion coefficient D_a, is produced by cells at rate μ and decays at rate δ. These equations classically show self-organisation, allowing a dispersed population to aggregate into one or more clusters. Assuming an average initial cell density, c_0, a simple analysis (e.g. see [43]) shows this occurs for:

$$\chi \mu c_0 > D_c \delta \, . \tag{3}$$

The above relationship reveals the heart of the mechanism responsible for aggregation: if the positive feedback in which cells produce their own chemoattractant is sufficiently strong, the stabilising elements of random movement and chemoattractant decay can be overcome. Models similar to the above have been proposed in numerous pattern formation processes, e.g. see [43]: in particular, we refer to [21] for an application to feather bud formation.

2.2. Chemotaxis model for feather patterning

We expand on the above ideas to formulate a chemotaxis-based model for feather patterning, based on the interactions between key cellular and molecular components described above and illustrated in Figure 1D. The model couples an imposed *priming wave* to a *patterning system* of cell/molecular components.

We focus on a rectangular portion of skin tissue, $\Omega = [0, L_x] \times [0, L_y]$, where for $(x, y) \in \Omega$ we set x to define the anterior-posterior (A-P) coordinate and y the medial-lateral (M-L) one. Note that given the *ex ovo* experimental context (e.g. Figure 1A), where tissue growth is negligible, we currently ignore any complexity due to embryonic expansion. We exploit the left/right symmetry of feather patterning by setting $y = 0$ to be the dorsal midline. Our mathematical model explicitly describes the spatio-temporal evolution of the following four variables:

- mesenchymal/dermal cell density, $m(x, y, t)$;
- the activated state of the epithelium, $e(x, y, t)$;
- FGF concentration, $f(x, y, t)$;
- BMP concentration, $b(x, y, t)$.

In addition, we model the initial "priming wave" through an imposed function $w(x, y, t)$. We note that while skin depth is not explicitly modelled, its three-dimensional structure is partially accounted for via the distinct locations of the cellular variables: the overlying epithelium is represented by its activation state, while dermal cells and diffusing molecules move within the underlying mesenchyme. Mathematically, our model is given by a system of equations of reaction-diffusion-advection type.

2.3. Priming wave

We consider the activity of an initial wave $w(x, y, t)$ that spreads through the tissue from medial to lateral fashion, priming the skin for patterning. For simplicity we do not currently model the molecular regulation of this process – this is left for future extensions – and impose a functional form as follows:

$$w(x, y, t) = \omega_1 \frac{1 + \tanh(\omega_2(t - y/\omega_3))}{2} . \tag{4}$$

Note in particular that w depends only on y and t, and not on any of the other model variables. This stipulates that the control of the priming wave is independent from the dynamics that govern the patterning system.

The above function generates a travelling-wave type profile that progressively shifts the skin from "un-primed" ($w = 0$) to "fully primed" ($w = \omega_1$ – full potential to pattern), beginning at the midline and spreading laterally. The parameters $\omega_{1,2,3}$ respectively control the strength (ω_1), steepness (ω_2) and speed (ω_3) of the wave as it spreads through the tissue: a formal basis for these parameters lies in the molecular control of the priming wave. For current purposes we have assumed any spread along the A-P axis is negligible.

2.4. Cell populations

2.4.1. Mesenchymal cells, $m(x, y, t)$

The dynamics of mesenchymal cells, $m(x, y, t)$, are taken as follows:

$$m_t = \nabla \cdot [D_m \nabla m - m\chi(m, f)\nabla f] . \tag{5}$$

The right hand side terms derive from cellular movement: the first specifies a diffusion term, representing an undirected (random) component to movement with constant motility coefficient D_m, while the second describes positive chemotaxis of dermal cells up FGF concentration gradients. For the chemotactic sensitivity function $\chi(m, f)$ we choose

$$\chi(m, f) = \alpha e^{-\gamma m} ,$$

where α measures the chemotactic strength coefficient and $e^{-\gamma m}$ acts as a counteraction to "overcrowding" (with coefficient γ) by reducing chemotactic movement when cells become increasingly clustered (for other possibilities see [43]).

The basic formulation here excludes mesenchymal cell kinetics: this is clearly a simplification, where dermal cell proliferation is likely to continue up to condensation. We do not account for this in the initial model, but do extend simulations later to include mesenchymal cell kinetics.

2.4.2. Epithelium activation

We do not model the epithelial cell population *per se*, rather we consider its local "activity state" through a variable $e(x, y, t) \in [0, 1]$, with $e(x, y, t) = 0$ defining fully inactive and $e(x, y, t) = 1$ maximum activity. A fully active epithelium is interpreted as one in which epithelial cells secrete FGF at a maximum rate, while fully inactive corresponds to zero FGF secretion. The equation governing the activity transition is given by

$$e_t = k_{\text{on}}(w, m)(1 - e) - k_{\text{off}}(b, m)e , \tag{6}$$

where the two terms on the right hand side respectively describe activation and inactivation, with rates $k_{\text{on,off}} \geq 0$. A trivial calculation shows that epithelial activity is bounded between 0 and 1, provided it is initially set within that range.

For the activation rate we take

$$k_{\text{on}}(w, m) = \kappa_1 w(x, y, t)h_1(m) + \kappa_2 h_2(m) . \tag{7}$$

The first term models the wave-dependent route to activation, with the activation rate depending on the mesenchymal cell density in the underlying dermis. Specifically, we assume activation increases with mesenchymal cell clustering, with the degree of clustering determined by a Hill function form:

$$h_1(m) = \frac{m^{p_1}}{{K_1}^{p_1} + m^{p_1}} . \tag{8}$$

The second term models the wave-independent route, again according to the level of clustering: this second path is motivated by the results of FGF-laden bead experiments, where the subsequent chemotaxis-induced clustering of mesenchymal cells at bead sites can promote activation and secretion of FGF by the overlying epithelium, even in regions not yet primed. We again take a Hill function form to define clustering:

$$h_2(m) = \frac{m^{p_2}}{{K_2}^{p_2} + m^{p_2}} . \tag{9}$$

Note that during parametrisation we will assume the wave-independent route plays a less significant role under "normal" conditions.

For the inactivation rate we take

$$k_{\text{off}}(b, c) = (1 - h_1(m))\,(\kappa_3 + \kappa_4 b) . \tag{10}$$

The above assumes that deactivation of the epidermis can occur in low mesenchymal cell density regions: BMP enhances the rate of deactivation from some baseline level. The presence of mesenchymal cell clusters blocks deactivation, modelled through the $(1 - h_1(m))$ term, so that clustering immediately below the epithelium both enhances (i.e. stimulates activation) and maintains (i.e. limits deactivation) its activity.

2.5. Molecular components

2.5.1. Fibroblast growth factor

Activated epithelium secretes FGF, which subsequently spreads along the epithelium-mesenchyme interface as a diffusible ligand. Specifically, we take

$$f_t = D_f \nabla^2 f + \kappa_{\text{FGF}} e - \delta_{\text{FGF}} f \,, \tag{11}$$

where D_f defines its diffusion coefficient, κ_{FGF} defines the secretion rate and δ_{FGF} is the decay rate.

2.5.2. Bone morphogenetic protein

We assume BMP is secreted by mesenchymal cells as a diffusible ligand:

$$b_t = D_b \nabla^2 b + \kappa_{\text{BMP}} h_3(m) m - \delta_{\text{BMP}} b \,, \tag{12}$$

where D_b defines its diffusion coefficient and δ_{BMP} is the decay rate. For production we assume BMP is secreted by the dermal cells at a rate that increases with their level of clustering, measured by

$$h_3(m) = \frac{m^{p_3}}{K_3^{p_3} + m^{p_3}} \,. \tag{13}$$

2.5.3. Summary

Summarising, the chemotactic model for feather patterning is given by

$$\begin{aligned} m_t &= \nabla \cdot \left[D_m \nabla m - \alpha m e^{-\gamma m} \nabla f \right] \,, \\ e_t &= (\kappa_1 w(x,y,t) h_1(m) + \kappa_2 h_2(m))(1-e) - (1 - h_1(m))\,(\kappa_3 + \kappa_4 b)\, e \,, \\ f_t &= D_f \nabla^2 f + \kappa_{\text{FGF}} e - \delta_{\text{FGF}} f \,, \\ b_t &= D_b \nabla^2 b + \kappa_{\text{BMP}} h_3(m) m - \delta_{\text{BMP}} b \,, \end{aligned} \tag{14}$$

with priming wave and density dependent functions

$$w(x,y,t) = \omega_1 \frac{1 + \tanh(\omega_2 (t - y/\omega_3))}{2} \text{ and } h_i(m) = \frac{m^{p_i}}{K_i^{p_i} + m^{p_i}} \,. \tag{15}$$

The model is closed with appropriate initial conditions and boundary conditions, as outlined in Appendix A. We further perform a nondimensional scaling (see Appendix A) and use the scaled form of equations in the results that follow.

3. Results

3.1. Linear stability analysis

Linear stability analysis (LSA) is employed to understand the model's innate capacity to pattern, as well as determine any constraints placed on cell density, chemotactic potential, molecular synthesis rates etc. Details are provided in Appendix B and here we summarise the principal results. LSA shows that the

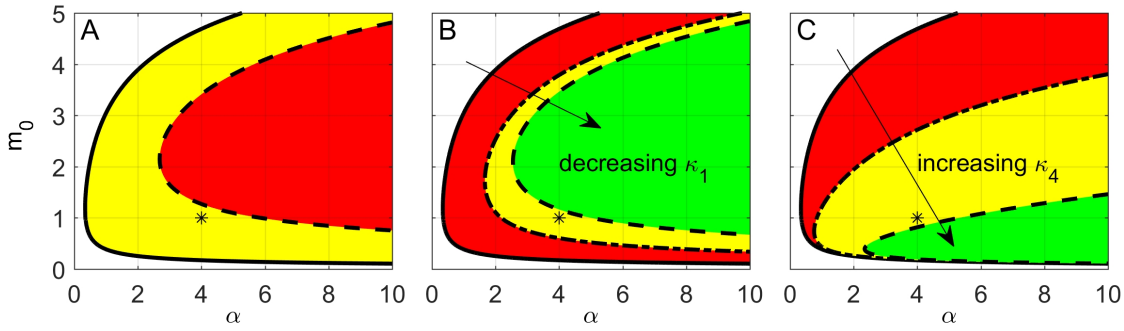

Figure 2: Predicted parameter space for patterning, with patterning regions indicated by colour-coded shading. (A) (α, m_0) parameter spaces for primed ($w = \omega_0$), and unprimed ($w = 0$) tissues. Union of red and yellow shaded zones (enclosed by solid black line) shows the region for primed tissue, while just the red zone (enclosed by dashed black line) shows the region for unprimed tissue. (B) Impact of changing κ_1 (epithelium activation rate): decreasing κ_1 shrinks the parameter space, with curves in the direction of the arrow corresponding to $\kappa_1 = 0.05$ (solid black line), 0.005 (dashed black line) and 0.0005 (dash-dotted black line). (C) Impact of changing κ_4 (BMP-induced epithelium inactivation rate): increasing κ_4 shrinks the parameter space, with curves in the direction of the arrow corresponding to $\kappa_4 = 1$ (solid black line), 10 (dashed black line) and 100 (dash-dotted black line). Other parameters set as default in Table A.1, with black stars indicating the position of the full default (nondimensional) parameter set.

model can generate spatial patterns through a positive feedback mechanism in which activated epithelium secretes FGF to induce chemotactic-mediated clustering of dermal cells, which in turn further activates the epithelium. If this process is sufficiently strong it overcomes the stabilising processes of diffusion, decay and BMP-induced inactivation of the epithelium. In line with experiments, blocking dermal cell movement/chemotaxis eliminates any pattern forming capability and demonstrates that chemotaxis is a critical driver, precluding that an alternative (activator-inhibitor based) path to pattern formation occurs. Either blocking epithelium activation or forcefully imposing widespread activation also prevents pattern formation, demonstrating that the epithelium requires tuning between ubiquitous over/under activity. Overall, these findings highlight the necessary interaction between dermal and epidermal layers for patterning.

A more nuanced understanding follows from parameter space plots for pattern formation. In Figure 2A we mark the patterning space regions corresponding to (i) "fully-primed skin", and (ii) "unprimed skin". Patterning of either primed or unprimed skin is dependent both on the strength of the chemotactic response and some critical dermal density, consistent with classical chemotaxis models and in line with experiments showing that a sufficiently dense dermis is necessary for patterning (e.g. [33]). Unprimed tissue also patterns, but only under significantly higher dermal cell densities. The parameter space plots indicate pattern disappearance for excessively high densities, where a crowded dermis inhibits movement into focussed aggregations.

The role of epithelium activation/inactivation is shown in Figure 2B-C. In Figure 2B we alter the wave-dependent activation rate (κ_1). Decreasing (increasing) this parameter restricts (expands) the patterning space, so that low (high) values of κ_1 would require a larger (smaller) chemotactic sensitivity or dermal cell density to induce patterning. A similar effect is observed by altering FGF secretion rates, with decreased (increased) secretion contracting (expanding) the parameter space. Figure 2C considers the rate of BMP-induced inactivation of epithelium (κ_4): increasing (decreasing) the sensitivity of epithelium to BMP shrinks (expands) the parameter space. Similar trends are obtained by increasing/decreasing the rate of BMP synthesis, which can be achieved through ubiquitously over/underexpressing *BMP*, where the model predicts that sufficiently high overexpression will prevent placode formation, in line with experiments (e.g.

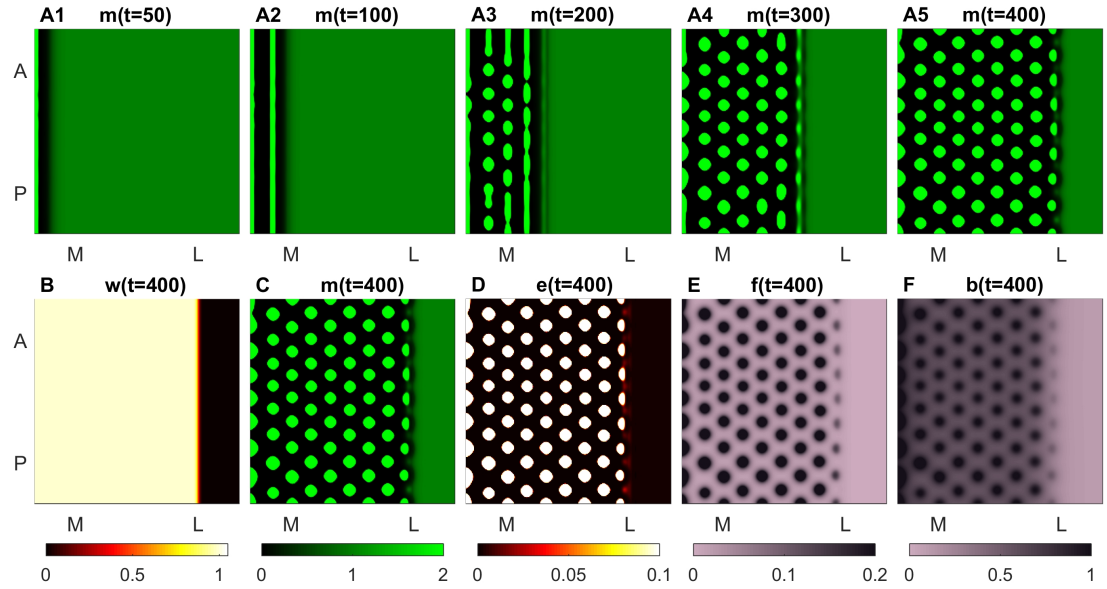

Figure 3: Representative simulation showing spatio-temporal patterning in the model. Each frame shows the spatial variation across medial-lateral (M-L) and anterior-posterior (A-P) axes for key model variables. (A) Emerging spatial pattern of dermal condensates (mesenchymal cell density, m) plotted at nondimensional times $t = 50, 100, 200, 300, 400$. Black to green colormap indicates increasing mesenchymal cell density. (B-F) Spatial distribution of each model variable at the end of a simulation run ($t = 400$). Left to right shows (B) priming wave (w), (C) mesenchymal cell density (m), (D) epithelium activity (e), (E) FGF (f) and (F) BMP (b). Distinct colormaps employed according to the form of variable: white/black for activity levels (priming wave and epithelium), black to green for cell densities (mesenchymal cells) and purple to black for molecular levels (FGFs and BMPs). Numerical simulations carried out as described in Appendix C, using the default nondimensional parameter set (Table A.1) on the scaled model for a domain of dimensions 20×20..

[9, 31]).

3.2. Spatio-temporal patterning

We numerically explore the full wave/patterning model to explore spatio-temporal characteristics of pattern formation (see Appendix C for details of numerical approach). In Figure 3 we observe the emergence of hexagonally-arranged mesenchymal cell condensates, with each new placode row appearing laterally to that most recently formed. Correlated with each condensate, we observe an activated epithelium and peaks of FGF and BMP concentration.

We note that in the simulations the initial row takes somewhat longer to form than later rows: forming the first row involves breaking the quasi-uniform initial state, whereas later rows can be guided by the "template" generated by earlier rows. While the artificially symmetric nature of the *in silico* study (e.g. regular geometry, minimal environmental stochasticity etc) may compound this slower formation, it is also possible that the unique positioning of the first row (along the dorsal midline, above structures such as the neural tube) may generate some form of pre-patterning template not reflected in the current model.

3.3. Sensitivity/Robustness

We employ a parameter sensitivity analysis to explore the robustness/sensitivity of patterning sequence in the face of (moderate) parameter perturbations. Specifically, we consider the impact of systematically

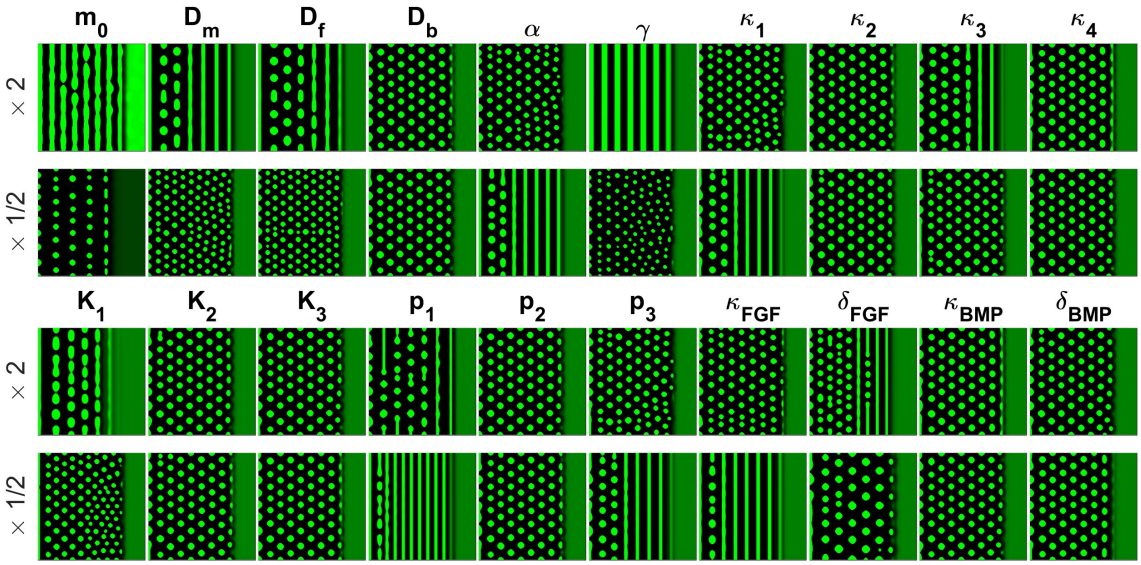

Figure 4: Parameter sensitivity analysis. Each model parameter has been changed by a factor of 2 or 1/2 from its value in Table A.1 and the spatial mesenchymal cell density m is plotted at the end of the simulation run (t = 400). Note that in all simulations we use the same colorscale (black to green for low to high cell density) for ease of comparison. All other details as in Figure 3.

perturbing each *dimensional* parameter, multiplying its default value (Table A.1) by 2 ("×2") or 0.5 ("×0.5") and leaving the other parameters unaltered. We note that given the default parameter set, none of these perturbations will displace the system outside the patterning space, as predicted by the stability analysis: thus, some form of pattern is still expected. Figure 4 shows the final solution following each perturbation. Many perturbations produce minimal change to the patterning outcome, suggesting that broadly the model is relatively robust. More significant perturbations tend to fall into two main classes: smaller and less regular primordia, or larger and often striped/fused primordia. Examples of the former include decreasing D_m, D_f or increasing α, all of which impact on chemotactic migration of mesenchymal cells into clusters: for example, decreasing FGF diffusion acts to sharpen chemoattractant gradients, while increasing α improves the chemotactic sensitivity of cells. Several parameters lead to an increased tendency towards stripes: such instances seem to result from a reduction in the tendency towards pattern – for example, decreasing FGF production rate or decreasing α directly impacts on the strength of the chemotactic response – so that cells have less time to resolve into focussed aggregates. Stripes are typically aligned along the emerging rows, a likely effect of the artificially high symmetry in the idealised model.

3.4. Localised exogenous delivery of BMP/FGF

We apply specific perturbations to the model to test the capacity of the model to predict particular experimental outcomes. Here we focus on altering the spatial molecular distribution pattern via exogenous localised addition of FGF and BMP. Specifically we consider *in silico* bead experiments, where FGF/BMP-laden beads are placed on the developing skin. Corresponding laboratory experiments are shown in Figure 5A-C, where beads are placed in developing skin tissue according to the positions of the white circles. Figure 5B illustrates the addition of BMP-laden beads: there is considerable local displacement of the pattern, with a strong suppression of primordia pattern formation in the vicinity of the bead. Figure 5C illustrates the

addition of FGF-laden beads: for beads placed in advance of the wave we observe the onset of clustering of dermal cells near the bead through chemotaxis. This process acts to deplete the surrounding pool of dermal cells, so that the arrangement of *de novo* forming primordia as the priming wave passes becomes distorted. Mathematically, we can recreate these experiments through an additional source term in the right-hand side of one of the molecular variables. For example, for FGF we would take:

$$f_t = D_f \nabla^2 f + s(x, y, t) + \kappa_{\mathrm{FGF}} e - \delta_{\mathrm{FGF}} f \,,$$

where $s(x, y, t)$ is the source of FGF. An equivalent addition can be made to the BMP equation. To model small circular beads we take

$$s(x, y, t) = \sum_{i=1}^{n} \begin{cases} \sigma_i & \text{if } \sqrt{(x - x_i)^2 + (y - y_i)^2} \leq r_i \,\&\, t \geq t_i \\ 0 & \text{otherwise} \end{cases} \,,$$

which models the addition of n circular beads of radii r_i, coordinates (x_i, y_i), at times t_i and with concentrations σ_i. In the simulations presented here, two identical beads are introduced at the same time with the same concentration but at different locations. At the time of initial implantation both beads are placed in unprimed tissue regions.

Figures 5D-E demonstrate the capacity of the model to replicate the experimental observations. Figure 5D plots the evolving mesenchymal cell density under the addition of BMP-soaked beads. The beads have little impact prior to the arrival of the priming wave, but once primed suppression of primordia is observed: primordia do not form in the vicinity of beads due to high levels in exogenous BMP preventing epithelium activation. Moreover, the surrounding arrangement of primordia is distorted by the BMP beads. We remark that these results are dosage dependent: for lower-dosed beads, the suppression may be negligible with the additional BMP insufficiently concentrated to block normal patterning. Figure 5E shows the corresponding simulations under FGF beads. At bead sites we observe an induced chemotactic accumulation of mesenchymal cells prior to the arrival of any priming wave. We remark that this increased density subsequently invokes localised epithelium activity and FGF secretion, artificially inducing an early primordium at the site of the bud but incapable of inducing secondary buds in the unprimed skin that surrounds it. As the patterning process reaches the bead we observe perturbations to primordia arrangement, a consequence of the localised depletion of dermal cells. We note again that these observations will be dosage-dependent, with lower concentrations potentially unable to induce a bud.

3.5. Incorporating cell proliferation

Simulations above have been performed for uniform initial densities, however experimental data suggests a significant medial-lateral variation in cell density at different stages of primordia development (Figure 1B). At the onset of bud patterning mesenchymal cell density is highest at the dorsal midline and decreases laterally. As development proceeds, cell densities rise laterally in a manner approximately consistent with the passage of the priming wave, such that the average cell density along each row is roughly the same at the time of their arrangement into buds. We suppose that proliferation along the rows slows substantially over time, so that there is little further increase in cell density once clusters are forming. Formally this could be tested by calculating the mean cell counts along a row/presumptive row in the stages prior to and during clustering.

To model this density distribution we modify the model to include:

- an initial, exponentially decreasing cell density distribution from medial to lateral, $m(x, y, 0) = m_0 e^{-\beta y}$, with other variables varying in a similar manner according to their steady state values;

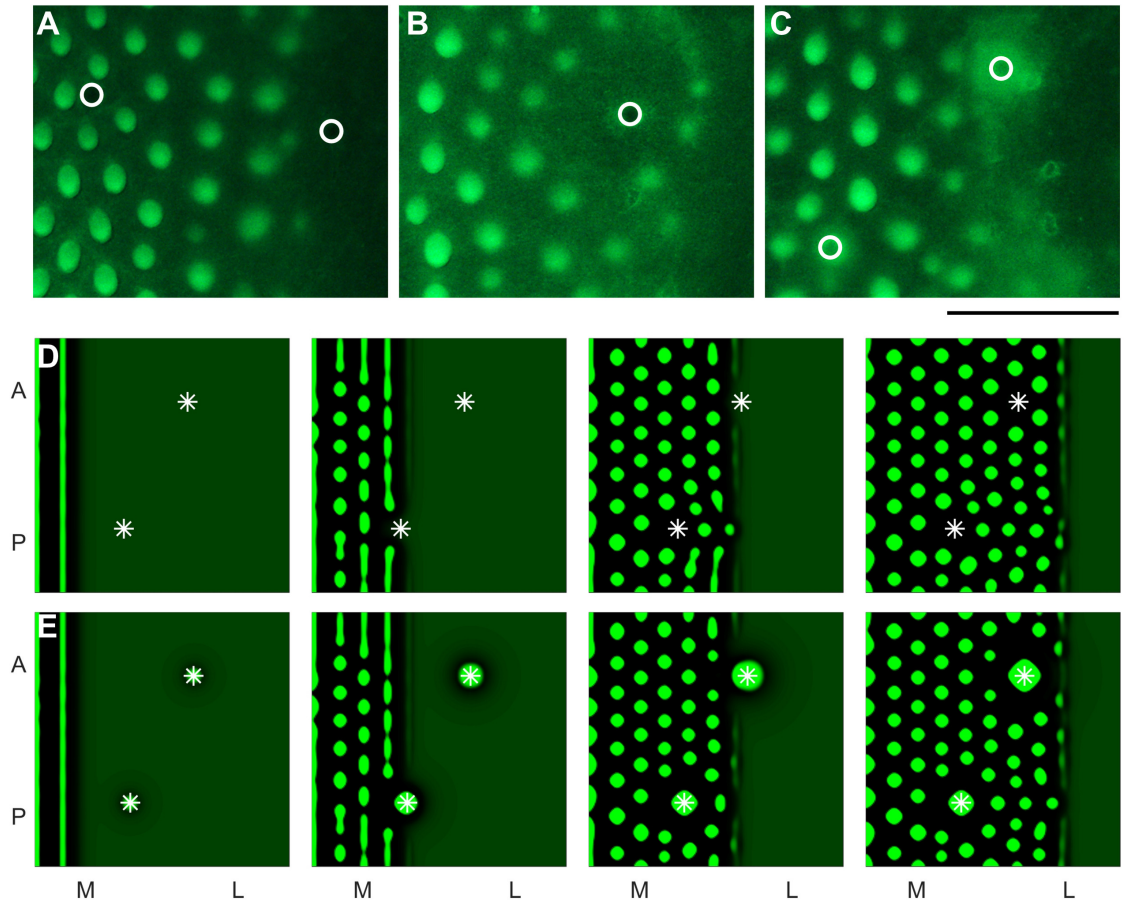

Figure 5: Localised delivery of BMP or FGF protein affects primordium placement. (A-C) E6.5 dorsal skin treated with protein coated beads and cultured for 72 hours, with position of beads denoted by white circles. (A) Primordium formation and arrangement unaffected by the presence of a bovine serum albumin (BSA) coated bead; (B) BMP coated beads create zones of inhibition in the surrounding region, suppressing primordia formation and arrangement; (C) FGF coated beads induce chemotactic attraction of dermal cells. This reduces the cell pool in the local area and hence the final arrangement of primordia. E6.5 dorsal tract skin explants prepared from GFP chicken embryos, with dermal condensates reflected by intense green. Scale bar indicates 1 mm, midline = left of images. (D-E) In silico bead implacement experiments. Beads (white stars) initially placed in primordia free regions, with dermal cell density shown during subsequent development (we plot m at $t = 100, 200, 300, 400$): (D) BMP beads; (E) FGF beads. Numerical details as in Figure 3, with additional bead parameters $r_i = 0.2, t_i = 0$ for $i = 1, 2$, $(x_1, y_1) = (15, 7.5), (x_2, y_2) = (5, 12.5)$ and (D) $\sigma_i = 250$, (E) $\sigma_i = 0.1$.

- a time-dependent proliferation of mesenchymal cells, so that the m-equation becomes

$$m_t = D_m \nabla^2 m - \nabla \cdot (\alpha m e^{-\gamma m} \nabla f) + r(t) m \,,$$

  with proliferation rate $r(t) = r_0(1 - w(x, y, t)/\omega_1)$.

In the above, mesenchymal cell proliferation depends on the priming wave, though we remark that we do not have a specific basis for choosing this: the form of $r(t)$ was phenomenologically chosen to ensure that any cell proliferation becomes negligible once the tissue is primed along a particular row and clusters are beginning to emerge. Numerous mechanisms could control cell proliferation, from components of the priming wave or patterning system to direct contact-inhibition between cells as they become clustered [44]. In terms of default values for the introduced parameters we remark that m_0 is taken as previously, β is estimated from the rate of decrease in cell density at the onset of patterning and $r_0 = \beta \times \omega_3$: the latter ensures that the average cell density along each presumptive row is (approximately) the same by the time placodes begin to form.

Figure 6A shows a simulation of the model under the inclusion of mesenchymal cell proliferation. Clearly we obtain the same orderly row-by-row generation of feather buds observed previously and consistent with *in vivo* pattern formation, suggesting that the model is relatively robust with respect to introducing more realistic cellular kinetics. Moreover, our amended model now allows predictions through *in silico* experiments. Specifically we simulate the *in silico* inhibition of cell proliferation via setting $r(t) = 0$ for $t \geq t_{\text{block}}$, where t_{block} defines the time that cell proliferation is blocked. Figures 6B-C show the results for $t_{\text{block}} = 100$ and 0 respectively. Blocking cell proliferation does not totally inhibit the formation of feather buds, but the number of rows that form is severely impacted: nearer the midline, where the mesenchymal cell density has risen sufficiently high, rows of buds form as normal while more lateral regions fail to produce feather buds. The inability of lateral regions to pattern under proliferation blocking highlights the need for a sufficiently dense dermis.

4. Discussion

We have developed a mathematical/computational model for spatio-temporal patterning of feather primordia. The model provides a formal test of the mechanism for feather patterning process, as proposed in Figure 7. The capacity of the model to replicate spatio-temporal patterning both in normal skin and under a variety of perturbations suggest that it represents a plausible mechanism for this pattern formation process. A regularly laid-out array of placodes is generated by an advancing "priming wave" that raises the inherent patterning capacity of the skin, the latter via chemotaxis-based self organisation. The formation of feather primordia in advancing waves, initiating from the midline on the dorsum, has long been noted [34]. In parallel with this work we have, in experimental studies aimed at defining the role of specific signalling pathways, identified a signalling protein produced in a spreading wave coincident with the wave of feather formation. This factor stimulates FGF production and determines the region of initiation of feather patterning [39], represented here by action of the priming wave.

Our previous modelling [31, 3] for FGF-BMP mediated modelling of primordia formation relied on a classical Turing/AI mechanism of Gierer-Meinhardt [7] type, where FGF and BMP operate as activators and inhibitors that directly (or indirectly) regulate each other's activity. As also shown in other studies (e.g. [23, 30]), these mechanisms are highly capable of both replicating and predicting feather patterning, so why move to a more complicated model? Firstly, the new model shifts towards a more mechanistic approach: we specifically account for key cellular components (epithelium and dermal cells) and explicitly

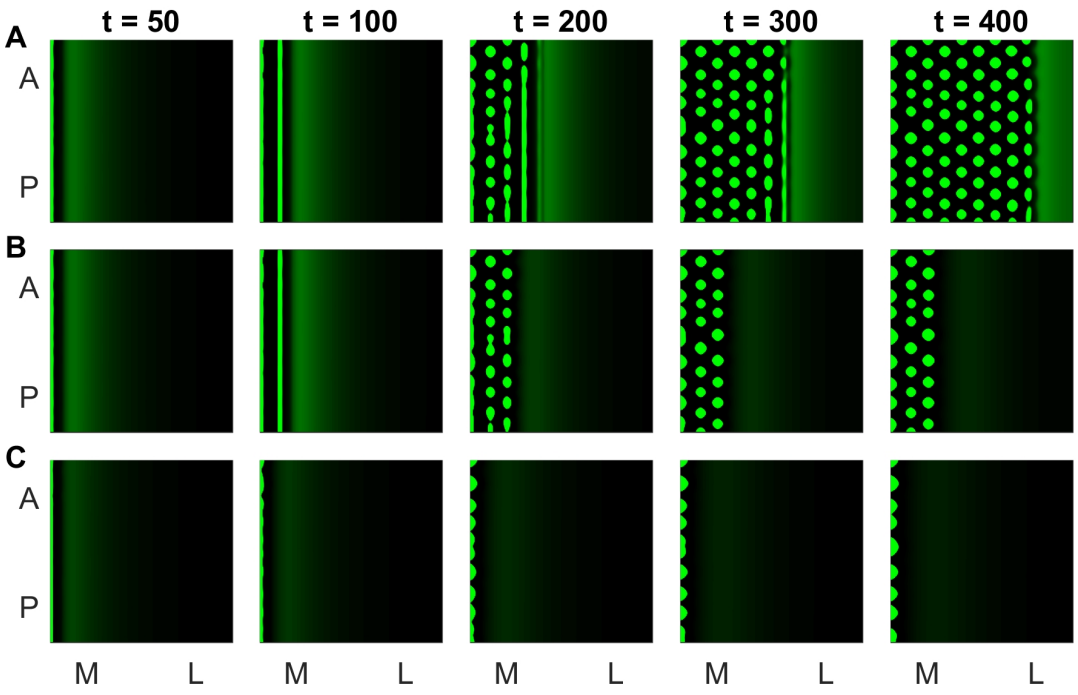

Figure 6: Incorporation of cell proliferation and an initial medial-lateral decrease in cell density. In each frame we plot the mesenchymal cell density (m) at the times indicated. (A) "Normal" scenario, showing the regular generation of feather bud rows in medial to lateral fashion. (B-C) In silico simulation of blocked cell proliferation. Cell proliferation is blocked at either (B) $t = 100$ or (C) $t = 0$. Blocking cell proliferation does not prevent the patterning of existing dermal cells into buds, but the subsequent number of formed rows is greatly depleted: once the existing mesenchymal cells have organised into buds, no more buds will form. Numerical simulations/parameters as in Figure 3 with $r_0 = 0.01$.

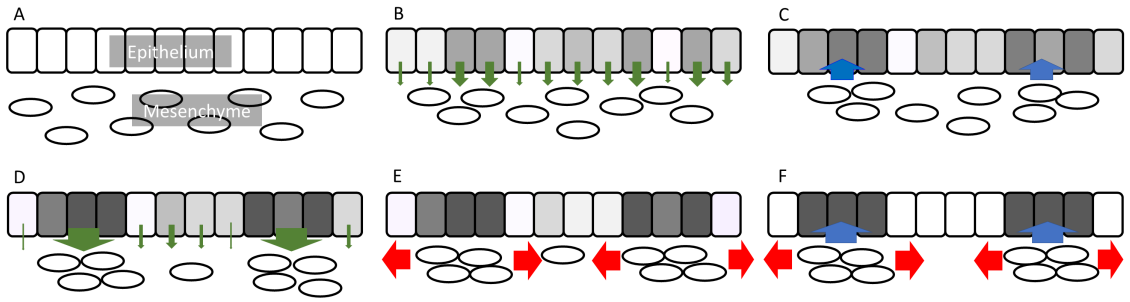

Figure 7: Schematic showing the mechanism by which the model gives rise to a patterned skin. A, an initially homogeneous skin is composed of a tightly packed epithelium underlaid by loosely populated dermis; B, a priming wave increases epithelium activity (shaded cells), resulting in a lowish levels of FGF secretion (green/down-pointing arrows); C, FGF-mediated chemotaxis results in loose dermal clusters at sites of FGF maxima, with clusters further upregulating overlying epithelium activity (blue/up-pointing arrows); D, higher activity increases FGF secretion and chemotactic clustering; E, high density dermal clusters secrete BMP, which diffuses through the surrounding mesenchyme (red/side-pointing arrows) and shuts down epithelium activity between clusters; F, the consequence is an alternating pattern between inactivated epithelium and low dermal density and activated epithelium underlaid by dermal condensates.

incorporate directed cell migration. Consequently, we can test specific experiments that target cell behaviour, such as the impact of blocking cell migration or proliferation (c.f. Figure 6). Secondly, the model's behaviour reflects recent experimental observations where cluster formation is found to anticipate the expression of any early gene markers for primordia [38]. Thirdly, the model does not rely on an underlying molecular network capable of Turing-type pattern formation on its own. We do not rule this out, however clear evidence of a direct (or indirect) molecular-signalling based autocatalysis in FGF is lacking. In the present model this feature is indirectly mediated through chemotaxis inducing a relocalisation of cells that subsequently upregulates epithelial activity.

Various works have considered the role of cell movement. A number of studies [22, 24, 25, 26, 38] proposed mechanochemical based models for feather patterning, where the organisation of cells clusters is driven through mechanical interactions between cells, extracellular fibres and other components. While these models are often less analytically/numerically convenient, they remain promising lines for enquiry. More directly relevant is the work of [30], who in an interdisciplinary study explored a coupled Turing-type/chemotaxis model to explain pattern formation, although there the underlying driver for the patterning process was the AI system. In [21] a simple cell/chemoattractant chemotaxis model was used to explain pattern formation, although there was no extension to consider the potential role of other key players such as BMPs, FGFs etc.

Classical chemotaxis models of the form (1-2) are well known for their complex spatio-temporal phenomena (e.g. see [45]), e.g. "aggregate merging" in which two clusters condense into a single cluster due to their mutual attraction. In the context of feather primordia, such events may be undesirable due to the subsequent loss of regular pattern. Simulations of the more detailed model (14) suggest that these are relatively rare events, at least within the timeframe of the study, although occasional merging does occur. The extra robustness of the more detailed chemotaxis model appears to stem from two factors: (i) the intermediary role of a fixed and static epidermis that actually produces the chemoattractant; and (ii), the inhibitory action of BMP that shuts down chemoattractant production in the interplacode zone. Nevertheless merging

can still occur and it is plausible to suppose that additional processes may act to suppress such behaviour, for example the presence of an undiscovered self-reinforcing mechanism in the FGF loop. Intriguingly, timelapse recordings of mesenchymal condensate formation suggests that aggregates do form close to each other, but subsequently move apart in an apparent act of cluster-cluster repulsion [39]. Such repulsion could theoretically result from a further chemorepulsion process whereby clusters also secrete a repelling agent; attraction-repulsion systems have been shown to generate and maintain stable multiple aggregates in extended chemotaxis models (e.g. see [46]). Chemorepulsion has been identified in early chick development [19], although at the level of individual cells rather than clusters and not during feather stages.

The present study has focussed on an *ex ovo* setting, where tissue growth/deformation can be neglected. *In vivo*, of course, tissue growth can heavily impact on patterning processes, such as the well documented phenomenon of "peak insertion" observed in Turing type models (e.g. see [47]). For chemotaxis based self organisation models tissue growth does not necessarily lead to such insertions, but rather can act to prevent merging and hence provide a stabilising element, e.g. see [48]. Yet, the precise patterning effects can be subtle and a more detailed investigation into how growth may specifically impact on patterning should be a point of focus in future studies.

The current study has been of "proof of concept" nature: qualitative rather than quantitative testing that the proposed model generates feather-type pattern formation. Based on the (nondimensional) spacing between primordia and the (nondimensional) time interval between newly forming rows (Figure 3) and converting back to dimensional units (Appendix A), parameters that would correspond to the approximate 200-300 μm spacing and 6-8 hourly interval observed *in vivo* would be of the order of 10 minutes for half-lives and 10^{-7} cm^{2}s^{-1} for BMP diffusion coefficients, the latter lying within ranges for estimated BMP diffusion coefficients in zebrafish [50, 49]. Given the model's seeming robustness to parameter perturbations we could also expect a reasonably broad variation about these values. Nevertheless, obtaining biological estimates and constructing a more quantitative modelling approach could increase the predictive power of the model, for example by eliminating candidate processes that prove "too slow" to pattern within developmental timescales [12].

The last two decades have provided compelling evidence that Turing/AI networks operate during morphogenetic processes ([9, 27, 10, 11, 51, 15, 13, 31, 14, 16, 12]). Yet definitively showing this is far from clearcut, as illustrated by the current model: while our model includes substances with "activator-like" (FGF) and "inhibitor-like" (BMP) properties, respectively promoting or suppressing pattern formation, it is actually chemotaxis that drives pattern formation, rather than a purely chemical/molecular driven process. Yet we cannot rule out that an AI process may occur, and a challenge for theoreticians and experimentalists alike is to devise methods to differentiate between distinct model viewpoints (e.g. see [4]). Complicating this considerable challenge further is the intriguing prospect that both chemical-based and mechanical-based patterning systems may simultaneously be present, as recently observed in follicle specification [12].

Acknowledgements: We would like to thank Franziska Matthäus for comments on an earlier draft of this manuscript. This work was supported by BBSRC grants BB/J017124/1 and BB/P013732/1, as well as a Visiting Professorship award to KJP by the Politecnico di Torino.

Appendix A. Initial, Boundary Conditions and Nondimensionalisation

Our chemotactic model for feather patterning is given by the system (14)–(15). To close the system, we impose initial and boundary conditions as follows:

- Boundary conditions. At the boundaries we set no-loss (zero-flux) boundary conditions, i.e. no material loss/gain across the domain edges:

$$\mathbf{n} \cdot [D_m \nabla m - \chi_0 m e^{-\gamma m} \nabla f] = \mathbf{n} \cdot \nabla f = \mathbf{n} \cdot \nabla b = 0\,,$$

  where $\mathbf{n}$ defines the outer unit norm on the boundary, $\partial\Omega$, of the domain.

- Initial conditions may change for some specific simulations, however generally:
  - ee set a uniform initial mesenchymal cell density, m_0, perturbed by a small spatially random component ($\xi(x, y)$, normalised to yield zero mean), i.e. $m(x, 0) = m_0 + \xi(x, y)$;
  - we set other variables at random perturbations of the inactive tissue uniform steady state level (see Appendix B.1).

The large set of model parameters can be somewhat reduced through nondimensionalisation. Specifically, we scale with:

$$m = m^*/\gamma\,, \quad f = \frac{\kappa_{\mathrm{FGF}}}{\delta_{\mathrm{BMP}}} f^*\,, \quad b = \frac{\kappa_{\mathrm{BMP}}}{\gamma\delta_{\mathrm{BMP}}} b^*\,, \quad t = \frac{t^*}{\delta_{\mathrm{BMP}}} \quad \mathbf{x} = \sqrt{\frac{D_b}{\delta_{\mathrm{BMP}}}}\mathbf{x}^*$$

We note that as an "activity state" e is already nondimensional, and therefore not included in the above scalings. We substitute into the model equations, define dimensionless parameters as in Table A.1 and, after dropping the stars for notational convenience, obtain:

$$m_t = d_m \nabla^2 m - \nabla \cdot (\alpha m e^{-m} \nabla f)\,, \tag{A.1}$$

$$e_t = (\kappa_1 w(x, y, t) h_1(m) + \kappa_2 h_2(m))\,(1 - e) - (1 - h_1(m))\,(\kappa_3 + \kappa_4 b)\,e\,, \tag{A.2}$$

$$f_t = d_f \nabla^2 f + e - \delta f\,, \tag{A.3}$$

$$b_t = \nabla^2 b + h_3(m) m - b\,, \tag{A.4}$$

with functional forms

$$w(x, y, t) = \omega_1 \frac{1 + \tanh(\omega_2(t - y/\omega_3))}{2} \quad \text{and} \quad h_i(m) = \frac{m^{p_i}}{K_i^{p_i} + m^{p_i}}, i = 1, 2, 3\,. \tag{A.5}$$

Paucity of quantitative data precludes formal parameter estimation. Given the current aim of testing the model's capacity to qualitatively recapitulate the dynamics of placode formation, we simply chose parameters at a "default set", applying certain considerations for relative values as follows:

- Mesenchymal cells are relatively motile, yet are expected to have a considerably lower diffusion coefficient than molecular species. FGF is released by the tightly packed epithelium, as opposed to straight into the loose dermis as for BMP, and is thus taken to have a more restricted diffusion to BMP. Hence, we assume $D_m < D_f < D_b$. However, we also remark that similar results can be obtained if $D_b = D_f$.
- Epithelium activation is assumed to occur on a slower timescale than inactivation: activation requires upregulating the machinery leading to FGF upregulation and secretion, whereas inactivation could simply involve shutting down the extracellular transport of FGF. Hence, $\kappa_{1,2} \ll \kappa_{3,4}$.
- Wave-independent activation of the epithelium is assumed to play a much less significant role than wave-dependent activation and only becomes significant at high dermal cell densities. Hence we set $K_1 < K_2$ and $\kappa_1 > \kappa_2$.
- Molecular decay rates are assumed to be approximately equal, i.e. $\delta = 1$, and on the same order as epithelium inactivation.

Parameter	Interpretation	Dimensionless version	Default value
m_0	Average mesenchymal density	$m_0^* = m_0/\gamma$	1.0
D_m	Random cell motility coefficient	$d_m = D_m/D_b$	0.01
D_f	FGF diffusion coefficient	$d_f = D_f/D_b$	0.1
D_b	BMP diffusion coefficient	Scaled out	–
χ_0	Chemotactic sensitivity coefficient	$\alpha^* = \alpha_0\kappa_{\mathrm{FGF}}/D_b\delta_{\mathrm{BMP}}$	4.0
γ	Crowding coefficient	Scaled out	–
κ_1	Wave-dependent activation rate	$\kappa_1^* = \kappa_1/\delta_{\mathrm{BMP}}$	0.05
κ_2	Wave-independent activation rate	$\kappa_2^* = \kappa_2/\delta_{\mathrm{BMP}}$	0.025
κ_3	BMP-independent inactivation rate	$\kappa_3^* = \kappa_3/\delta_{\mathrm{BMP}}$	1.0
κ_4	BMP-dependent inactivation rate	$\kappa_4^* = \kappa_4\kappa_{\mathrm{BMP}}/\gamma\delta_{\mathrm{BMP}}^2$	1.0
K_1	Clustering coefficient for h_1	$K_1^* = K_1\gamma$	1.0
K_2	Clustering coefficient for h_2	$K_2^* = K_2\gamma$	3.0
K_3	Clustering coefficient for h_3	$K_3^* = K_3\gamma$	5.0
$p_{1,2,3}$	Hill function coefficients	$p_{1,2,3}$	2
κ_{FGF}	FGF secretion rate	Scaled out	–
κ_{BMP}	BMP secretion rate	Scaled out	–
δ_{FGF}	FGF decay rate	$\delta = \delta_{\mathrm{FGF}}/\delta_{\mathrm{BMP}}$	1.0
δ_{BMP}	BMP decay rate	Scaled out	–
ω_1	Priming wave strength	ω_1	1.0
ω_2	Priming wave steepness	$\omega_2^* = \omega_2/\delta_{\mathrm{BMP}}$	5.0
ω_3	Priming wave speed	$\omega_3^* = \omega_3/\sqrt{D_b\delta_{\mathrm{BMP}}}$	0.04

Table A.1: List of parameters, their meaning, dimensionless form and default value for simulations. Note that in subsequent descriptions, we employ the terms given in the above table when also referring to nondimensional forms, even though the latter depend on additional system parameters.

Appendix B. Stability analysis and patterning criteria

We perform a standard linear stability analysis (e.g. see [52]) of (A.1-A.5) where, for simplicity, we restrict to a single spatial dimension (x) and assume an infinite domain. Effectively this provides an analysis into patterning along a presumptive row of feather buds. The analysis for bounded domains in two dimension is straightforward, yet demands extra attention due to the stated boundary conditions; these complications add little and are therefore ignored.

Appendix B.1. Steady states

In the absence of cell kinetics the total mesenchymal population is conserved and the uniform steady state (m_s, e_s, f_s, b_s) is dictated by the initial mean population density, i.e. $m_s = m_0$. Straightforward algebra reveals that the BMP steady state is given by $b_s = h_3(m_0)m_0$ while the FGF steady state depends on the epithelial activity, i.e. $f_s = e_s/\delta$. Epithelium activity at steady state depends on the balance between activation and inactivation, i.e.

$$e_s = \frac{k_{\text{on}}}{k_{\text{on}} + k_{\text{off}}},$$

which, in addition to the dependence on m and b, depends on the state of the priming wave.

For uniform steady states we consider the following tissue scenarios:

- *Unprimed tissue*, where $w(x, y, t) = 0$. In this case we obtain steady state

  $$(m_0, e_u, e_u/\delta, m_0 h_3(m_0)),$$

  where e_u will be given by

  $$e_u = \frac{\kappa_2 h_2(m_0)}{\kappa_2 h_2(m_0) + (1 - h_1(m_0))(\kappa_3 + \kappa_4 m_0 h_3(m_0))}.$$

- *Fully primed tissue*, where $w(x, y, t) = \omega_1$. In this case we obtain steady state

  $$(m_0, e_p, e_p/\delta, m_0 h_3(m_0)),$$

  where e_p satisfies

  $$e_p = \frac{\omega_0\kappa_1 h_1(m_0) + \kappa_2 h_2(m_0)}{\omega_0\kappa_1 h_1(m_0) + \kappa_2 h_2(m_0) + (1 - h_1(m_0))(\kappa_3 + \kappa_4 m_0 h_3(m_0))}.$$

Note that it is trivial to show $e_p \geq e_u$, i.e. the epithelium (at steady state) is more active for a primed tissue.

Appendix B.2. Stability analysis

We substitute

$$(m(x,t), e(x,t), f(x,t), b(x,t)) = (m_s, e_s, f_s, b_s) + (\tilde{m}(x,t), \tilde{e}(x,t), \tilde{f}(x,t), \tilde{b}(x,t))$$

into equations (A.1-A.4), where $(\tilde{m}(x,t), \tilde{e}(x,t), \tilde{f}(x,t), \tilde{b}(x,t))$ define small perturbations. Ignoring any subsequent nonlinear terms, we make the standard ansatz of solutions of the form $\tilde{m}, \tilde{e}, \tilde{f}, \tilde{b} \sim e^{i\nu x + \lambda t}$ where, for the unbounded domain case, $\nu \in \mathbb{R}$. Here ν denotes the wavenumber, with corresponding wavelength $= 2\pi/\nu$. Patterns can be expected to form when the steady state is unstable, which occurs if at least one

eigenvalue λ has a positive real part for at least one (nonnegative) value of ν. The eigenvalues are determined by the stability (or Jacobian) matrix which, for equations (A.1-A.4), will be given by

$$A = \begin{pmatrix} -d_m\nu^2 & 0 & \alpha m_0 e^{-m_0}\nu^2 & 0 \\ a_{21} & -a_{22} & 0 & -a_{24} \\ 0 & a_{32} & -d_f\nu^2 - a_{33} & 0 \\ a_{41} & 0 & 0 & -d_b\nu^2 - a_{44} \end{pmatrix}.$$

The coefficients a_{ij} are given as

$$\begin{aligned} a_{21} &= (w\kappa_1(1-e_s) + (\kappa_4 b_s + \kappa_3)e_s)\, h_1'(m_s) + \kappa_2 h_2'(m_s)\,; \\ a_{22} &= wk_1 h_1(m_s) + \kappa_2 h_2(ms) + (1 - h_1(m_s))(b_s\kappa_4 + \kappa_3)\,; \\ a_{23} &= (1 - h_1(ms))\kappa_4 e_s\,; \\ a_{32} &= 1\,; \\ a_{33} &= \delta\,; \\ a_{41} &= h_3(m_s) + m_s h_3'(m_s)\,; \\ a_{44} &= 1\,; \end{aligned}$$

where $w = 0$ for the unprimed steady state and $w = \omega_1$ for the primed steady state. We note that $0 \leq h_i(m_s) < 1$, $h_i'(m_s) \geq 0$ and $0 \leq e_s \leq 1$: the a_{ij}'s are therefore nonnegative for all (biologically relevant) parameters. The characteristic equation for the eigenvalues is a fourth order polynomial of the form

$$\lambda^4 + c_1(\nu^2)\lambda^3 + c_2(\nu^2)\lambda^2 + c_3(\nu^2)\lambda + c_4(\nu^2) = 0\,, \tag{B.1}$$

where:

$$\begin{aligned} c_1 &= (d_f + d_m + 1)\nu^2 + a_{22} + a_{33} + a_{44}\,; \\ c_2 &= (d_f d_m + d_f + d_m)\nu^4 + \Big(a_{22}(d_f + d_m) + a_{33}(d_m + 1) + a_{44}(d_m + d_f)\Big)\nu^2 \\ &\quad + a_{22}a_{33} + a_{22}a_{44} + a_{33}a_{44}\,; \\ c_3 &= d_f d_m \nu^6 + \Big((a_{22} + a_{44})d_f d_m + a_{22}(d_f + d_m) + a_{33}d_m\Big)\nu^4 \\ &\quad + \Big(a_{22}a_{33}d_m + a_{22}a_{44}d_f + a_{22}a_{44}d_m + a_{33}a_{44}d_m - a_{32}a_{21}\alpha m_0 e^{-m0}\Big)\nu^2 + a_{22}a_{33}a_{44}\,; \\ c_4 &= \nu^2\Big(a_{22}d_f d_m\nu^4 + \Big(a_{22}a_{44}d_f d_m + a_{22}a_{33}d_m - \alpha m_0 e^{-m_0}a_{21}a_{32}\Big)\nu^2 \\ &\quad + a_{22}a_{33}a_{44}d_m - \alpha m_0 e^{-m0}(a_{21}a_{32}a_{44} - a_{41}a_{32}a_{24})\Big)\,. \end{aligned} \tag{B.2}$$

Appendix B.2.1. Simplified scenarios

Explicitly computing the eigenvalues is generally nontrivial for a fourth order characteristic equation. However, under certain simplifications it can become straightforward.

Zero chemotaxis of mesenchymal cells. In this case $\alpha = 0$ and eigenvalues are:

$$\lambda_1 = -d_m\nu^2\,, \quad \lambda_2 = -a_{22}\,, \quad \lambda_3 = -d_f\nu^2 - a_{33}\,, \quad \lambda_4 = -d_b\nu^2 - a_{44}\,.$$

None of the above are positive and patterning is not predicted under this scenario. In particular, we note that this precludes pattern formation arising in the model from a non-chemotactic self-organising mechanism, such as activator-inhibitor based: the absence of any form of self-activation (or cross-activation) within the signalling interactions between FGF, BMP and epithelium preclude this.

Zero activation of epithelium. Here, $\kappa_1 = \kappa_2 = 0$ and $e = 0$ at the steady state. Consequently, $a_{21} = a_{24} = 0$ and eigenvalues are as for the zero chemotaxis case. Again, patterning is not predicted.

Zero inactivation of epithelium. Here, $\kappa_3 = \kappa_4 = 0$ and $e = 1$ at the steady state, corresponding to a fully activated epithelium everywhere. We have $a_{21} = a_{22} = a_{24} = 0$ and obtain eigenvalues

$$\lambda_1 = -d_m\nu^2\,, \lambda_2 = -\nu^2 - a_{44}\,, \lambda_3 = -d_f\nu^2 - a_{33}\,, \lambda_4 = 0\,.$$

Again, patterning is not predicted.

Zero production of FGF. Note that this in fact corresponds to setting $\kappa_{\mathrm{FGF}} = 0$ in the original (dimensional) equations: the specific nondimensionalisation cannot be used, yet a modified version leads to an equivalent A, but with $a_{32} = 0$. Eigenvalues are as for the zero chemotaxis case and patterning is not predicted.

Appendix B.2.2. General scenario

The Routh-Hurwitz conditions provide a necessary and sufficient set of conditions under which the real parts of the eigenvalues are negative: for the fourth order polynomial above, these conditions correspond to

$$c_i > 0\,, c_1c_2 - c_3 > 0 \text{ and } c_1c_2c_3 - c_3^2 - c_1^2c_4 > 0\,,$$

and breaching any of the above (for at least one value of ν) corresponds to an unstable steady state. While c_1 and c_2 are clearly nonnegative, whether the other conditions satisfy the above is less clear cut and a comprehensive analysis would clearly be both analytically intricate (if not intangible) and of limited usefulness. We therefore restrict to a more limited study by concentrating solely on the $c_4(\nu^2)$ term, subsequently employing numerical studies to support a contention that this is the predominant path to pattern formation, at least near the default parameter set.

Straightforward algebra shows that c_4 can be negative for (positive) k if at least one of the following two inequalities is satisfied:

$$\alpha m_0 e^{-m0} a_{32}\,(a_{21} - a_{41}a_{24}/a_{44}) > d_m a_{22} a_{33}\,; \tag{B.3}$$

$$\begin{aligned}(\alpha m_0 e^{-m_0} a_{21}a_{32} - a_{22}a_{44}d_f d_m - a_{22}a_{33}d_m)^2 > \\ 4a_{22}d_f d_m(a_{22}a_{33}a_{44}d_m - \alpha m_0 e^{-m_0} a_{32}(a_{21}a_{44} - a_{41}a_{24}))\,.\end{aligned} \tag{B.4}$$

The above condition (B.3) clearly demonstrates the positive feedback process under which patterning can be achieved: chemotactic-mediated (α) accumulation of mesenchymal cells at FGF maxima stimulates further FGF secretion (a_{32}) through clustering-dependent activation of the epithelium (a_{21}): if this is sufficiently strong, the steady state is destabilised. Notably, BMP-induced inactivation of the epithelium can shut down this mechanism (a_{41}, a_{24}).

The capacity of the above relationships to characterise the patterning space is demonstrated by plotting the parameter regions enclosed by (B.3) and (B.4) and then comparing against a numerically-calculated region; the latter is found by explicitly solving (B.1–B.2) as we discretely step through a range of ν and sweep through a two-dimensional portion of parameter space, marking each parameter space location for which the leading eigenvalue of (B.1) has a positive real component for at least one positive value of ν.

Figure B.8A plots the results for a region of (m_0, α) space: in (A1) the black solid curve marks the numerically-determined boundary for the patterning region (to the right of the curve) while red-dot-dashed and green-dashed curves respectively describe the boundaries generated by inequalities (B.3) and (B.4). The union of the two regions generated by (B.3) and (B.4) almost exactly matches the numerically-determined region. Note that using only one of the inequalities is insufficient (obvious for inequality (B.3), where the red-dot-dashed curve clearly fails to track the solid black curve along its upper portion).

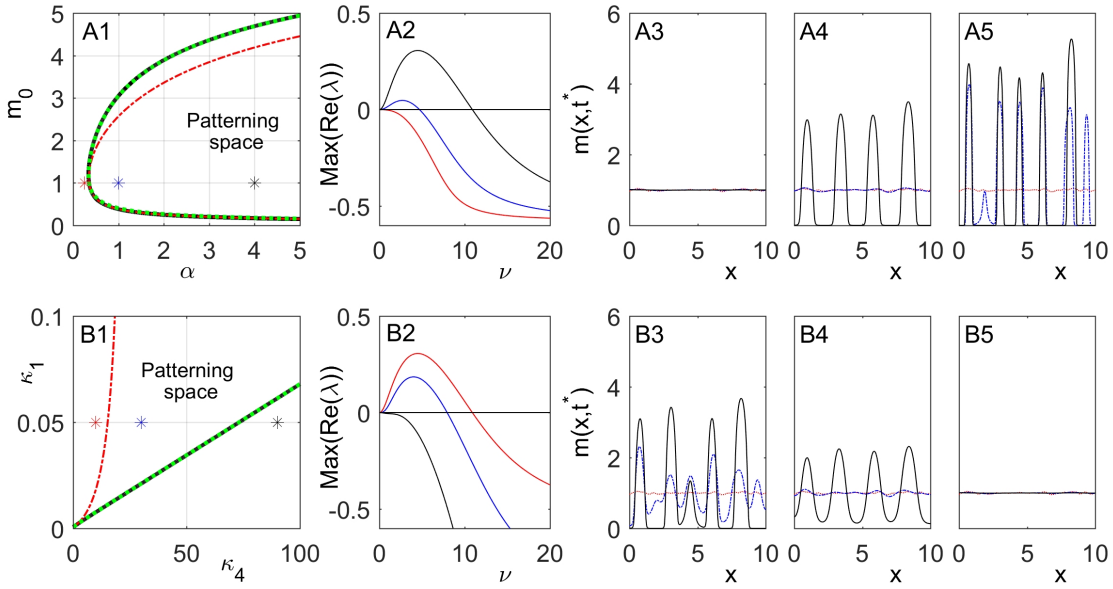

Figure B.8: Patterning space, dispersion relationships and 1D numerical simulations. (A1) Numerically and predicted patterning space, over a portion of $\alpha - m_0$ parameter space: (black solid) the boundary of the numerically-determined patterning space; (red-dashed) boundary formed by (B.3); (green-dashed) boundary by (B.4). Starred points mark: (red) $(0.25, 1)$, (blue) $(1, 1)$ and (black) $(4, 1)$. (A2) Dispersion relations for the starred locations in (A1), with (red curve) $(0.25, 1)$, (blue) $(1, 1)$ and (black) $(4, 1)$. (A3-A5) Numerical solutions of the model for (A3) $(\alpha, m_0) = (0.25, 1)$, (A4) $(\alpha, m_0) = (1, 1)$ and (A5) $(\alpha, m_0) = (4, 1)$; other parameters in Table A.1 and initial conditions comprised of perturbations from the primed steady state. Numerical simulations plot the density profile $m(x, t^*)$ at times (red dotted) $t^* = 0$, (blue dashed) $t^* = 25$ and (black solid) $t^* = 250$. (B1-B5) A similar analysis of $\kappa_1 - \kappa_4$ parameter space. Here the starred locations marked in (B1) and employed in (B2-B4) represent the (κ_1, κ_4) points (red) $(10, 0.05)$, (blue) $(30, 0.05)$ and (black) $(90, 0.05)$.

In (A2) we plot dispersion relations ($\lambda - \nu$ plots) for the three starred locations marked in (A1): moving into the patterning region results in a finite range of positive ν for which the leading eigenvalue of the stability matrix has a positive real component. In (A3-A5) we plot 1D numerical simulations that correspond to the starred locations, initiating the system with a small random perturbation about the uniform steady state solution. The numerical results support the linear stability analysis: for locations outside the patterning region, perturbations decay and the solutions evolve to the uniform steady state (A3); inside the patterning region, we observe growing perturbations that evolve into spatially periodic condensations of mesenchymal cells (A4-A5). The simulations here reveal the critical nature of chemotaxis, with pattern formation only occurring above a critical chemotactic sensitivity parameter α.

Figure B.8B shows the results from a similar study as we sweep across $\kappa_1 - \kappa_4$ space. Again, the union of the regions generated by inequalities (B.3) and (B.4) correlates with the numerically-determined patterning space. The simulations confirm the patterning capacity of the model system for appropriate parameter values. Note that these simulation highlight the inhibitory effect of BMP, with large sensitivity to BMP (large κ_4) resulting in the obliteration of patterning.

Appendix C. Numerical methods

Numerical simulations invoke a Method of Lines approach, where the system of equations given by (14) and (15) is first discretised spatially to obtain a high-dimensional system of time-dependent ODEs that are subsequently integrated over time. For the spatial-discretisation we employ a standard central difference scheme for diffusion terms, and an upwinding scheme for the chemotactic terms: the latter invokes a mixed order flux-limiting method, which switches from third to first order as necessary to ensure positivity of solutions [53]. Time integration has involved crosschecking between both a variable time stepping algorithm and an explicit Euler method. Simulations have been further checked through utilising different grid resolutions, time steps and error tolerances. Except where specifically stated otherwise, all simulations employ the dimensionless set of parameters in Table A.1 and consider a dimensionless field of size 20×20, with initial and boundary conditions as described in Appendix A.

[1] R. Baker, S. Schnell, P. Maini, Waves and patterning in developmental biology: vertebrate segmentation and feather bud formation as case studies, Int. J. Dev. Biol. 53 (5-6) (2009) 783–794.

[2] H. G. Othmer, K. Painter, D. Umulis, C. Xue, The intersection of theory and application in elucidating pattern formation in developmental biology, Math. Mod. Nat. Phen. 4 (2009) 3–82.

[3] K. J. Painter, G. S. Hunt, K. L. Wells, J. A. Johansson, D. J. Headon, Towards an integrated experimental-theoretical approach for assessing the mechanistic basis of hair and feather morphogenesis, Interface Focus 2 (2012) 433–450.

[4] T. W. Hiscock, S. G. Megason, Mathematically guided approaches to distinguish models of periodic patterning, Development 142 (2015) 409–419.

[5] L. Wolpert, Positional information and the spatial pattern of cellular differentiation, J. Theor. Biol. 25 (1) (1969) 1–47.

[6] A. M. Turing, The chemical basis of morphogenesis, Phil. Trans. Roy. Soc. Lond. Series B, Biol. Sci. 237 (1952) 37–72.

[7] A. Gierer, H. Meinhardt, Theory of biological pattern formation, Kybernetik 12 (1) (1972) 30–39.

[8] L. A. Segel, J. L. Jackson, Dissipative structure: an explanation and an ecological example, J. Theor. Biol. 37 (3) (1972) 545–559.

[9] H. S. Jung, P. H. Francis-West, R. B. Widelitz, T. X. Jiang, S. Ting-Berreth, C. Tickle, L. Wolpert, C. M. Chuong, Local inhibitory action of BMPs and their relationships with activators in feather formation: implications for periodic patterning, Dev. Biol. 196 (1998) 11–23.

[10] M. P. Harris, S. Williamson, J. F. Fallon, H. Meinhardt, R. O. Prum, Molecular evidence for an activator-inhibitor mechanism in development of embryonic feather branching, Proc. Nat. Acad. Sci. USA 102 (33) (2005) 11734–11739.

[11] S. Sick, S. Reinker, J. Timmer, T. Schlake, Wnt and Dkk determine hair follicle spacing through a reaction-diffusion mechanism, Science 314 (2006) 1447–1450.

[12] J. D. Glover, K. L. Wells, F. Matthäus, K. J. Painter, W. Ho, J. Riddell, J. Johansson, M. Ford, C. A. B. Jahoda, V. Klika, R. L. Mort, D. J. Headon, Hierarchical patterning modes orchestrate hair follicle morphogenesis, PLoS Biol. 15 (2017) e2002117.

[13] S. W. Cho, S. Kwak, T. E. Woolley, M. J. Lee, E. J. Kim, R. E. Baker, H. J. Kim, J. S. Shin, C. Tickle, P. K. Maini, H. S. Jung, Interactions between Shh, Sostdc1 and Wnt signaling and a new feedback loop for spatial patterning of the teeth., Development 138 (2011) 1807–16.

[14] F. G. Sala, P. M. Del Moral, C. Tiozzo, D. A. Alam, D. Warburton, T. Grikscheit, J. M. Veltmaat, S. Bellusci, FGF10 controls the patterning of the tracheal cartilage rings via Shh, Development 138 (2011) 273–282.

[15] T. Nakamura, N. Mine, E. Nakaguchi, A. Mochizuki, M. Yamamoto, K. Yashiro, C. Meno, H. Hamada, Generation of robust left-right asymmetry in the mouse embryo requires a self-enhancement and lateral-inhibition system, Dev. Cell 11 (2006) 495–504.

[16] J. Raspopovic, L. Marcon, L. Russo, J. Sharpe, Digit patterning is controlled by a Bmp-Sox9-Wnt turing network modulated by morphogen gradients, Science 345 (2014) 566–570.

[17] E. F. Keller, L. A. Segel, Initiation of slime mold aggregation viewed as an instability, J. Theor. Biol. 26 (1970) 399–415.

[18] J. T. Bonner, The social amoebae: the biology of cellular slime molds, Princeton University Press, 2009.

[19] X. Yang, D. Dormann, A. E. Münsterberg, C. J. Weijer, Cell movement patterns during gastrulation in the chick are controlled by positive and negative chemotaxis mediated by FGF4 and FGF8, Dev. Cell 3 (2002) 425–437.

[20] A. Shellard, R. Mayor, Chemotaxis during neural crest migration, Sem. Cell & Dev. Biol. 55 (2016) 111–118.

[21] C. M. Lin, T. X. Jiang, R. E. Baker, P. K. Maini, R. B. Widelitz, C. M. Chuong, Spots and stripes: pleomorphic patterning of stem cells via p-ERK-dependent cell chemotaxis shown by feather morphogenesis and mathematical simulation., Dev. Biol. 334 (2009) 369–382.

[22] J. D. Murray, G. F. Oster, A. K. Harris, A mechanical model for mesenchymal morphogenesis, J. Math. Biol. 17 (1983) 125–129.

[23] B. N. Nagorcka, The role of a reaction-diffusion system in the initiation of skin organ primordia. 1. the first wave of initiation., J. Theor. Biol. 121 (1986) 449–475.

[24] B. N. Nagorcka, V. S. Manoranjan, J. D. Murray, Complex spatial patterns from tissue interaction - an illustrative model, J. Theor. Biol. 128 (1987) 359–374.

[25] L. J. Shaw, J. D. Murray, Analysis of a model for complex skin patterns, SIAM J. Appl. Math. 50 (1990) 628–648.

[26] G. C. Cruywagen, P. K. Maini, J. D. Murray, Sequential pattern formation in a model for skin morphogenesis, IMA J. Math. Appl. Med. & Biol. 9 (1992) 227–248.

[27] T. X. Jiang, H. S. Jung, R. B. Widelitz, C. M. Chuong, Self-organization of periodic patterns by dissociated feather mesenchymal cells and the regulation of size, number and spacing of primordia., Development 126 (1999) 4997–5009.

[28] K. Patel, H. Makarenkova, H. S. Jung, The role of long range, local and direct signalling molecules during chick feather bud development involving the BMPs, follistatin and the Eph receptor tyrosine kinase Eph-A4., Mech. Dev. 86 (1999) 51–62.

[29] R. O. Prum, S. Williamson, Reaction-diffusion models of within-feather pigmentation patterning, Proc. Biol. Sci. 269 (2002) 781–792.

[30] F. Michon, L. Forest, E. Collomb, J. Demongeot, D. Dhouailly, BMP2 and BMP7 play antagonistic roles in feather induction., Development 135 (2008) 2797–2805.

[31] C. Mou, F. Pitel, D. Gourichon, F. Vignoles, A. Tzika, P. Tato, L. Yu, D. W. Burt, B. Bed'hom, M. Tixier-Boichard, K. J. Painter, D. J. Headon, Cryptic patterning of avian skin confers a developmental facility for loss of neck feathering., PLoS Biol. 9 (2011) e1001028.

[32] C. M. Chuong, C. Y. Yeh, T. X. Jiang, R. Widelitz, Module-based complexity formation: periodic patterning in feathers and hairs, Wiley Interdiscip. Rev. Dev. Biol. 2 (2013) 97–112.

[33] I. Olivera-Martinez, J. P. Viallet, F. Michon, D. J. Pearton, D. Dhouailly, The different steps of skin formation in vertebrates, Int. J. Dev. Biol. 48 (2004) 107–115.

[34] D. Davidson, The mechanism of feather pattern development in the chick. II. control of the sequence of pattern formation, J. Embryol. Exp. Morphol. 74 (1983) 261–273.

[35] M. W. Hughes, P. Wu, T. X. Jiang, S. J. Lin, C. Y. Dong, et al., In search of the golden fleece: unraveling principles of morphogenesis by studying the integrative biology of skin appendages, Integr. Biol. 3 (2011) 388–407.

[36] C. M. Lin, T. X. Jiang, R. B. Widelitz, C. M. Chuong, Molecular signaling in feather morphogenesis, Curr. Opin. Cell. Biol. 18 (2006) 730–741.

[37] K. L. Wells, Y. Hadad, D. Ben-Avraham, J. Hillel, A. Cahaner, D. J. Headon, Genome-wide SNP scan of pooled DNA reveals nonsense mutation in FGF20 in the scaleless line of featherless chickens., BMC Genomics 13 (2012) 257.

[38] A. E. Shyer, A. R. Rodrigues, Schroeder, G. G., E. Kassianidou, S. Kumar, H. R. M., Emergent cellular self-organization and mechanosensation initiate follicle pattern in the avian skin, Science Epub ahead of print (2017) doi: 10.1126/science.aai7868.

[39] W. Ho, *et al* and Headon, D. J., Interacting cellular and molecular waves drive gain and loss of high fidelity feather patterning (Working Title, In preparation).

[40] H. K. Song, S. H. Lee, G. P. F., FGF-2 signaling is sufficient to induce dermal condensations during feather development, Dev. Dyn. 231 (2004) 741–749.

[41] C. S. Patlak, Random walk with persistence and external bias, Bull. Math. Biophys. 15 (1953) 311–338.

[42] E. F. Keller, L. A. Segel, Model for chemotaxis, J. Theor. Biol. 30 (1971) 225–234.

[43] T. Hillen, K. J. Painter, A user's guide to pde models for chemotaxis, J. Math. Biol. 58 (2009) 183–217.
[44] H. Fisher, J. Yeh, Contact inhibition by colony formation, Science. 155 (1967), 581–582.
[45] K. J. Painter, T. Hillen, Spatio-temporal chaos in a chemotaxis model, Physica D 240 (2011) 363–375.
[46] M. Luca, A. Chavez-Ross, L. Edelstein-Keshet, A. Mogilner, Chemotactic signalling, microglia, and Alzheimer's disease senile placques: is there a connection?, Bull. Math. Biol. 65 (2003) 693–730.
[47] E. J. Crampin, E. A. Gaffney, P. K. Maini, Reaction and diffusion on growing domains: scenarios for robust pattern formation, Bull. Math. Biol., 61 (1999), 1093–1120.
[48] K. J. Painter, T. Hillen, Volume-filling and quorum-sensing in models for chemosensitive movement, Can. Appl. Math. Quart., 10 (2002), 501–43.
[49] J. Zinski, Y. Bu, X. Wang, W. Dou, D. Umulis, M. Mullins, Systems biology derived source-sink mechanism of BMP gradient formation, eLife 6 (2017) e22199.
[50] A. P. Pomreinke, G. H. Soh, K. W. Rogers, J. K. Bergmann, A. J. Blässle, P. üller, Dynamics of BMP signaling and distribution during zebrafish dorsal-ventral patterning, eLife 6 (2017) e25861.
[51] C. Mou, B. Jackson, P. Schneider, P. A. Overbeek, D. J. Headon, Generation of the primary hair follicle pattern., Proc. Natl. Acad. Sci. USA 103 (2006) 9075–9080.
[52] J. D. Murray, Mathematical Biology: II Spatial models and biomedical applications, Springer, 2003.
[53] W. Hundsdorfer, J. G. Verwer, Numerical solution of time-dependent advection-diffusion-reaction equations, Vol. 33, Springer, 2013.